Cold Welding — Theoretical Modeling of the Weld Formation

A new model simulates the cold welding process, including deformation of base metals and the resulting weld strength in similar and dissimilar metal welds

W. ZHANG AND N. BAY

ABSTRACT. Based on experimental investigations and an improved understanding of the mechanisms of weld formation in cold welding, a general theoretical model for weld strength in cold welding — earlier developed by Bay — has been extended and modified. The new model presented in this paper simulates the whole cold welding process, including the deformation of base metals and the resulting weld strength in welding similar, as well as dissimilar, metals. To verify the theoretical model, the calculated weld strengths are compared with experimental measurements. Good accordance is generally found, which shows the model is applicable.

Introduction

In the first two papers of the present series (Refs. 1, 2), comprehensive experimental investigations of the influence of alternative surface preparation methods and fractographic investigations of the weld formation were presented. It was shown that the mechanical properties of the cover layers may differ considerably depending on the type, the metal combination and on which metal they are applied (Refs. 1, 2). This will have a significant influence on the weld strength obtained, as experimentally observed in Ref. 1 and theoretically shown in this paper.

The weld strength in cold welding is rather difficult to predict because it is influenced by a great number of parameters. The first attempt was made by Vaidyanath, *et al.* (Ref. 3), and a simple theoretical model was proposed for the maximum weld shear strength that can be attained in cold welding. This model was later modified by Wright, *et al.* (Ref. 4). These two models were derived on the basis of weld fracture behavior but with no query as to the weld formation process. In the two models only one parameter, the total reduction, is taken into account. This will undoubtedly limit the application of the models. Furthermore, none of the models can predict the threshold deformation theoretically.

Almost at the same time as Wright, Bay (Refs. 5–7) developed a new theoretical model based on the essential considerations of the welding mechanisms. This became the first quantitative theory expressing the presence and the size of the threshold surface expansion for initiating cold welding.

It was realized that the weld formation in cold welding is rather complicated. Before cold welding, the metal surfaces are covered either by contaminant films or by strategic, brittle cover layers. During cold welding, the cover layers are first fractured due to deformation of the base metals and the virgin metal surfaces are exposed in the cracks. Then the exposed virgin metal is extruded through the cracks to meet the opposing metal surface and, finally, the welds are established where the virgin metal surfaces from both metals meet each other (Refs. 8–10).

This paper presents a theoretical modeling of the weld formation in cold welding including analysis of the deformation of base metals, as well as analysis of the extrusion of base metals through cracks in the cover layer taking into account the mechanical properties of the cover layer. The model is described in detail in Refs. 11–15.

KEY WORDS

Cold Welding
Cold Roll Welding
Aluminum
Copper
Steel
Theoretical Model
Weld Strength
Surface Exposure
Normal Pressure
Extrusion Pressure

General Model for Weld Strength

The metal surfaces usually are overlaid by cover layers or contaminant films. Cold welding can only be initiated and established in the areas of the contacting interface surfaces where exposed virgin surfaces on both sides are in direct contact with each other. Referring to the experimental observations of Conrad and Rice (Ref. 16), it was found that the weld strength obtained between absolutely clean surfaces is approximately equal to the compression stress applied in cold welding. This was later verified by Bay (Ref. 5) with a theoretical model of the asperity deformation in contacts between two rough surfaces. Based on this assumption, the effective normal pressure (p_B) acting on the portion of the interface where the uncovered areas of both surfaces are overlapping will be the true

W. ZHANG and N. BAY are with the Institute of Manufacturing Engineering, Technical University of Denmark, Lyngby, Denmark.

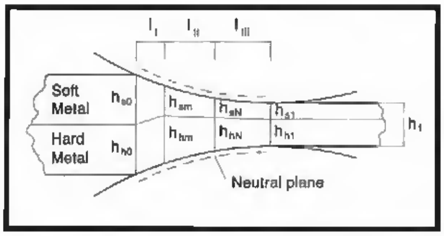

Fig. 1 — Deformation zone in compound plate rolling of two dissimilar metals.

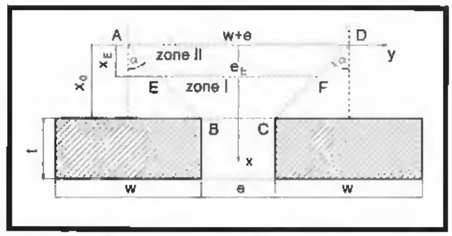

Fig. 2 — Geometry of the deformation zone of extrusion through cracks at interface.

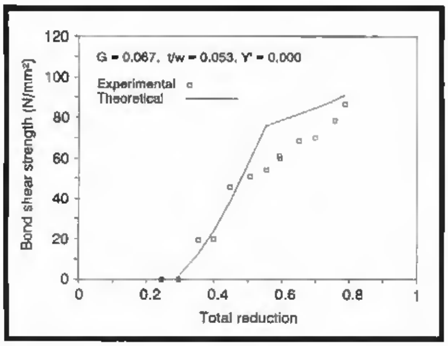

Fig. 3 — Calculated and experimental weld shear strength as a function of total reduction, Al-Al with one-sided electroless Ni plating (ACAD).

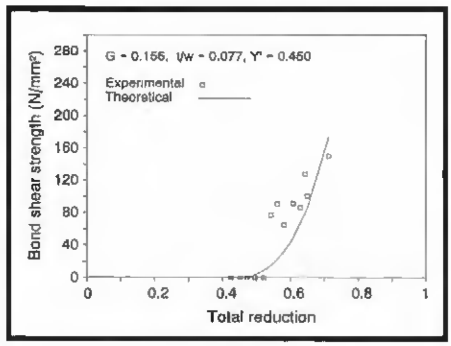

Fig. 4 — Calculated and experimental weld shear strength as a function of the total reduction, Cu-Cu with one-sided electroless Ni plating (CCCD).

weld strength. Thus, the nominal weld strength (σ_B) corresponding to the entire interface area will be

$$\sigma_B = \psi p_B \quad (1)$$

where ψ is the overlapping surface exposure. However, the weld strength obtained cannot increase as the effective pressure to infinity; the maximum weld strength obtained in cold welding will be the strength (flow stress σ_0) of the weaker base metal:

$$(\sigma_B)_{max} = \sigma_{0weak} \quad (2)$$

Equation 1 is the basic equation of the new theoretical model for weld strength. The weld strength will be calculated by estimating the overlapping surface exposure (ψ) and the effective normal pressure (p_B) for various surface preparations and different metal combinations.

The Overlapping Surface Exposure

The overlapping surface exposure is determined by calculating the true surface exposure of each metal at the interface, which is determined depending on the type of surface. The actual metal surfaces are classified into two types: metal surfaces with relatively thick cover layers and those with thin contaminant films. For the metal surface with cover layer, the true surface exposure (ψ_C) is calculated by the following equation:

$$\psi_C = \frac{A_1 - A_c}{A_1} = (1-G)Y \quad (3)$$

where A_1 is the surface area after deformation and A_c is the area remaining with the cover layer. Y is the nominal surface expansion

$$Y = \frac{A_1 - A_0}{A_1} \quad (4)$$

where A_0 is the initial surface area. G is the ductility of the cover layer, which is expressed by

$$G = \frac{Y - \psi_c}{Y} = 1 - \frac{\psi_c}{Y} \quad (5)$$

Equation 3 represents the percentage of the newly exposed virgin metal surface at the deformed interface between the two metals.

For the metal surface originally covered with contaminant films, the true surface exposure (ψ_F) is calculated by the following equation:

$$\psi_F = \frac{A_1 - A'}{A_1} = \frac{Y - Y'}{1 - Y'} \quad (6)$$

where A' is the threshold surface area necessary to expose virgin surface. Y' is the threshold surface expansion to initiate cold welding for metals with only contaminant films, which is defined as

$$Y' = \frac{A' - A_0}{A'} \quad (7)$$

The value of Y' for each metal with contaminant films only is determined by pilot welding experiments.

In a very special case, the scratch-brushed metal surface is a combination of the two types. The fraction (γ) of the surface area without cover layer can be estimated by SEM observations of the scratch-brushed surface (Refs. 6–10). Knowing this fraction parameter, the true surface exposure of the scratch-brushed surfaces can be calculated in two parts, and the same applies to the weld strength. The ductility (G) and the dimension ratio (t/w) of the cover layer in the case of the scratch-brushed surfaces were estimated with micrographs, knowing the fraction (γ) of the surface area without cover layer following a similar procedure described in Ref. 2.

In cold welding, virgin metal surfaces will be exposed on both of the opposing metal surfaces. However, welds can only be established in the portion where both of the virgin surfaces meet each other, that is, only the portion where the exposed metal surfaces are overlapping will contribute to the weld formation. The overlapping surface exposure is then calculated in the following two cases depending on the true surface exposures of the base metals.

If the true surface exposure of the two metals is the same, e.g., in cold welding of similar metals with the same surface layer, the surface layers on the two metal surfaces will fracture as one (or the cracks in the surface layers on both sides will develop correspondingly) due to the homogeneous deformation of the base metals and the heavy friction at the interface during deformation of the base metals. Thus, the overlapping surface exposure will be equal to the true surface exposure of each metal:

$$\psi = \psi_M \quad (8)$$

where ψ_M is the true surface exposure of any base metal.

Otherwise, if the true surface exposures are different, e.g., in cold welding of dissimilar metals or similar metals with different surface layers, the overlapping surface exposure will be equal to the multiplication of the true surface exposures of the two metals:

$$\psi = \psi_{M1}\psi_{M2} \quad (9)$$

where ψ_{M1} and ψ_{M2} are the true surface exposure of the two base metals.

The Effective Normal Pressure

The effective normal pressure also is calculated depending on the two surface types. For the metal surfaces with thin contaminant films only, the exposed virgin metal surfaces will immediately get into contact in the overlapped areas. The deformation pressure (p) will contribute unreduced to the weld formation (Refs. 6–10), that is,

$$p_{BI} = p \qquad (10)$$

For the metal surface with a thicker cover layer, welding cannot be established until the exposed virgin surfaces are extruded into the cracks of the fractured cover layer and brought into contact. The effective normal pressure contributing to the weld formation will be the remainder of the deformation pressure (p) after counteracting the extrusion pressure (p_E), thus,

$$p_{BE} = p - p_E \qquad (11)$$

where p is calculated by analysis of the deformation process, whereas p_E can be obtained by analysis of the extrusion of base metal through cracks in the cover layer (Refs. 6–10).

Deformation Pressure in Cold Welding

The deformation pressure is obtained by theoretical modeling of the metal forming process applied for cold welding. As an example, a theoretical modeling of the compound plate rolling in cold roll welding has been carried out. In cold roll welding, the two metals to be welded are rolled together and joined by plastic deformation and pressure.

Figure 1 is an illustration of the deformation zone in compound plate rolling. When two dissimilar metals with different yield stresses are rolled together, the softer metal will be deformed more than the harder metal, and the deformation of the softer metal will be initiated earlier than that of the hard metal in the roll gap.

Theoretical analysis of the deformation and pressure in the compound plate rolling process was carried out by using the Finite Difference Method (FDM). In the analysis, strain hardening of the metals is taken into account and a general friction model proposed by Wanheim and Bay (Ref. 17) is applied. This analysis provides the deformation pressure p and the surface expansion (Y) of the base metals at the weld interface along the roll gap. Besides, the individual thickness of each metal after cold roll welding can also be estimated. For further details about the analysis of the compound plate rolling, refer to Refs. 11–13.

Extrusion Pressure Necessary for Weld Formation

A theoretical analysis of the extrusion of the base metal through cracks in the

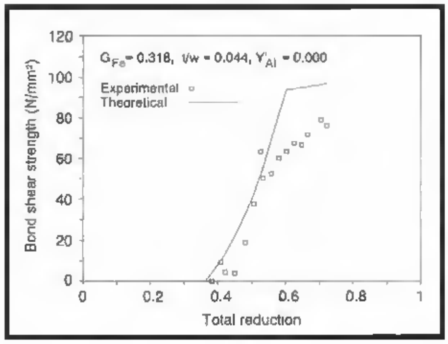

Fig. 5 — Calculated and experimental weld shear strength as a function of the total reduction. Al-steel with one-sided electroless Ni plating on steel (ADFC).

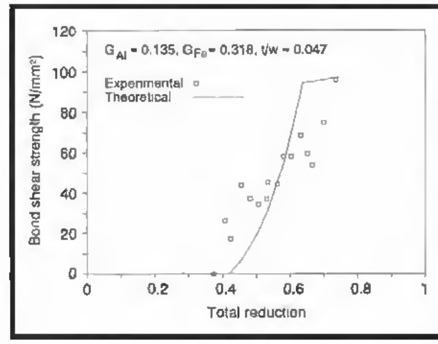

Fig. 6 — Calculated and experimental weld shear strength as a function of the total reduction. Al-steel with two-sided electroless Ni plating (ACFC).

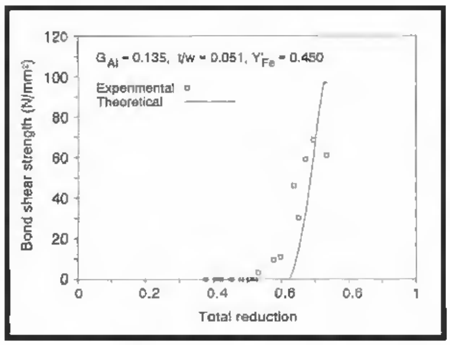

Fig. 7 — Calculated and experimental weld shear strength as a function of the total reduction, Al-Steel with one-sided electroless Ni plating on Al (ACFD).

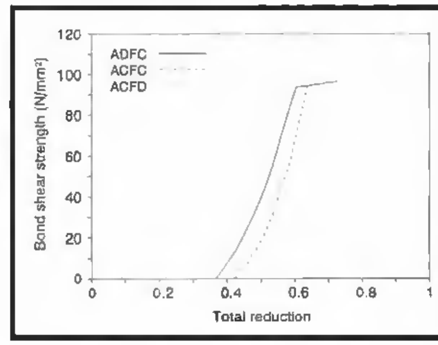

Fig. 8 — Calculated weld shear strength as a function of the total reduction, Al-steel with one- and two-sided electroless Ni plating.

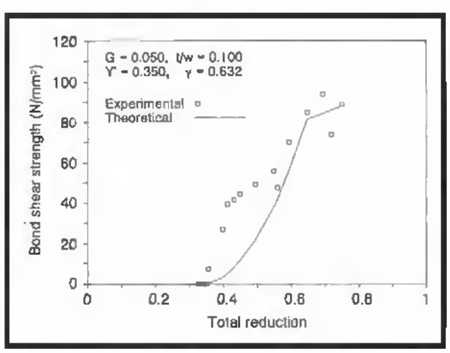

Fig. 9 — Calculated and experimental weld shear strength as a function of the total reduction, Al-Al with scratch-brushed surfaces (ABAB).

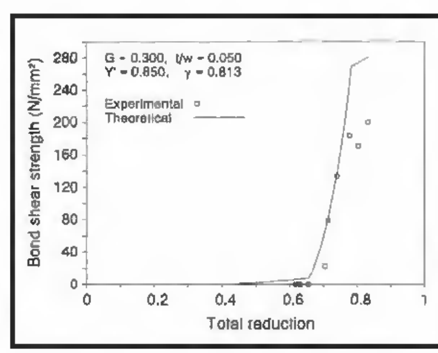

Fig. 10 — Calculated and experimental weld shear strength as a function of the total reduction, Cu-Cu with scratch-brushed surfaces (CBCB).

cover layer during cold welding is conducted to calculate the extrusion pressure necessary for weld formation. The extrusion process is treated as a plane strain deformation through multiple square dies (cracks act as extrusion dies).

Figure 2 shows an illustration of the deformation zone in extrusion of the base metal through cracks in the cover layer, assuming the material to form a dead zone along AB and CD. For simplicity, the deformation is considered to be homogeneous, *i.e.*, planes like EF remain planes. It is understood that the extrusion may not reach steady state conditions when the dimension ratio (t/w) of the fragments of cover layer is small enough, which means that after extrusion of the deformation zone (ABCD), the metal in zone I (EBCF) is extruded into the crack, whereas the metal in zone II (AEFD) is only extruded downward to the crack. When the dimension ratio (t/w) of the fragments is large enough, the extrusion will become complete, reaching steady state, which means zone II will disappear. The critical value of the dimension ratio (t/w) is calculated as follows:

$$\left(\frac{t}{w}\right)_c = \frac{1}{4\tan\alpha}\left(\frac{1}{(1-G)Y}+1\right) \qquad (12)$$

where G is the ductility of the cover layer, Y is the surface expansion of the base metal in rolling, and α is the estimated dead zone angle in the extrusion — Fig. 2. When the actual dimension ratio (t/w) of the fragments is smaller than this critical value, the extrusion is an incomplete process, otherwise it is a complete process.

The energy method is used for calculation of the extrusion pressure (Ref. 18). It is found that the extrusion pressure is dependent on the yield stress of the base metal (with work hardening), the surface expansion (Y) of the base metal, the dimension ratio (t/w) of the fragments of the cover layer and the ductility (G) of the cover layer. A detailed development of the theoretical model for the extrusion pressure is not presented here because it is a special metal forming problem. Refer to Refs. 11 and 14 for details.

Verification of the Theoretical Model

Based on the theoretical analysis, a software program named ROBO© has been developed to accomplish the calculations presented above. The general shape of the theoretical curve of the weld strength is shown as the solid line in Fig. 3. The weld strength starts at a threshold surface expansion, which is experimentally determined in the case of the metal surfaces with contaminant films only and theoretically predicted in the case of the metal surfaces with cover layers because of the necessity of extrusion of the base metals (Equation 11). At a certain surface expansion, the weld strength reaches the maximum, which is the flow stress of the weaker metal (Equation 2). To verify the theoretical model, calculated results are compared with the experimental data. Some examples are presented below.

Cold Welding of Similar Metals with Plating Layers

Figures 3 and 4 show the comparison of the theoretical and the experimental weld shear strength for cold welding Al-Al and Cu-Cu with one-sided electroless Ni plating as surface preparation. Good agreement is found in both cases, implying that the weld strength model is applicable for cold welding of similar metals.

Cold Welding of Dissimilar Metals with Plating Layers

Figures 5–7 show the comparison of the theoretical and the experimental weld shear strength for cold welding Al-steel with electroless Ni plating on alternative sides. Good agreement is generally found. Figure 8 shows a comparison of the theoretical weld shear strength curves in the three cases, which shows good agreement with the experimental results presented in the first paper of this series (Ref. 1). This implies that the weld strength model is applicable also for cold welding of dissimilar metals.

Cold Welding of Metals with Scratch-Brushed Surfaces

Figures 9 and 10 show the comparison of the theoretical and the experimental weld shear strength for cold welding of Al-Al and Cu-Cu with scratch-brushed surfaces. Reasonably good agreement is found, implying that the theoretical model also can be applied for cold welding of metals with scratch-brushed surfaces.

Conclusions

Based on the very considerable experimental results and the detailed analysis of the welding mechanisms, the theoretical analysis of the entire process of roll welding has been documented in a more general theoretical model together with the operating program (ROBO©). To the best of the authors' knowledge, this is the first general theoretical model ever developed for cold welding of dissimilar metals considering the incomplete extrusion of the base metal through cracks in the cover layer during weld formation.

The significant aspects of this general model are attributed to the following two factors: 1) the analysis of incomplete extrusion of the base metal through cracks in the cover layer during weld formation has for the first time been theoretically carried out taking into account the ductility of the cover layer and the geometry of the fragments of the cover layer, as well as the work hardening of the base metal; 2) the analysis of the compound plate rolling process and the introduction of the overlapping surface exposure have made it possible for the first time to apply a general model for roll welding of dissimilar metals.

Significant comparisons between the calculated results and the experimental data have been presented, which can be seen to show reasonably good accordance.

References

1. Zhang, W., and Bay, N. 1997. Cold welding — experimental investigation of the surface preparation methods. *Welding Journal* 76(8): 326-s to 330-s.

2. Zhang, W., and Bay, N. 1997. Cold welding — fractographic investigation of the weld formation. *Welding Journal* 76(9): 361-s to 366-s.

3. Vaidyanath, L. R., Nicholas, M. G., and Milner, D. R. 1959. Pressure welding by rolling. *British Welding Journal* 6(1): 13–28.

4. Wright, P. K., Snow, D. A., and Tay, C. K. 1978. Interfacial conditions and bond strength in cold pressure welding by rolling. *Metals Technology* (1): 24–31.

5. Bay, N. 1979. Cold pressure welding — the mechanisms governing bonding. *Journal of Engineering for Industry*. Transactions of the ASME 101(5): 121–127.

6. Bay, N. 1981. Cold pressure welding — a theoretical model for the bond strength. *The Joining of Metals: Practice and Performance*. Vol.2, Coventry, U.K., 47–62.

7. Bay, N., Clemensen, C., and Juelstorp, O. 1985. Bond strength in cold roll bonding. *Annals of the CIRP* 34 (1): 221–224.

8. Bay, N. 1983. Mechanisms producing metallic bonds in cold welding. *Welding Journal* 62(5): 137-s to 142-s.

9. Bay, N. 1985. Friction and Adhesion in Metal Forming and Cold Welding. D.Sc. thesis, Technical University of Denmark.

10. Bay, N. 1986. Cold welding. Part 1 — Characteristics, bonding mechanisms, bond strength. *Metal Construction* (6): 369–372.

11. Zhang, W. 1994. Bond Formation in Cold Welding of Metals. Ph. D. dissertation. Technical University of Denmark.

12. Zhang, W., and Bay, N. 1993. Numerical analysis of the cold roll bonding process. *Proc. 1st International Conference on Modelling of Metal Rolling Processes*. London, U.K. pp. 525–540.

13. Zhang, W., and Bay, N. Numerical Modelling of Compound Plate Rolling. To be offered for publication in *Journal of Materials Processing Technology*.

14. Zhang, W., and Bay, N. Calculation of the Extrusion Pressure for the Base Metal through Cracks of the Surface Cover Layer in Cold Pressure Welding. To be offered for publication in *Journal of Materials Processing Technology*.

15. Zhang, W., and Bay, N. A General Theoretical Model for the Bond Strength in Cold Pressure Welding. To be offered for publication in *Journal of Materials Processing Technology*.

16. Conrad, H., and Rice, L. 1970. The cohesion of previously fractured FCC metals in ultrahigh vacuum. *Metallurgical Transactions* 1:3019–3029.

17. Wanheim, T., and Bay, N. 1978. A model for friction in metal forming processes. Annals of the CIRP 27:189–194.

18. K. Lange, Ed. 1985. *Handbook of Metal Forming*. McGraw-Hill Book 12.1-12.33.

Effect of Thermal Aging on the Damping Properties of a Resistance Spot-Welded Acrylic-Cored Laminated Steel

The effect of thermal aging on the damping properties of a resistance spot-welded acrylic-cored laminated steel was investigated

BY P. C. WANG AND R. J. FRIDRICH

ABSTRACT. The concern over the thermal stability of polymer materials has led to studies on the damping properties of polymer-cored laminated steels used for reducing the structure-borne and engine noise of an automobile. In this study, we investigate the effects of spot weld nugget presence and thermal aging on damping properties of a resistance spot-welded acrylic-cored laminated steel. Damping properties were measured prior to and after specimen exposure to air at the Electrophoretic Priming Operation (ELPO) bake temperature of 180°C. Test results showed that damping system loss factor of the resistance spot-welded acrylic-cored laminated steel is dominated by shearing action within the acrylic core, and weld nugget presence has little influence. There is no significant change in system loss factor when the aging duration is increased to 0.5 h. Between 5- and 50-h exposure, system loss factors decreased. Scanning electron microscopy, thermal gravimetric, and differential scanning calorimetric analyses indicated that the decrease in system loss factor is likely caused by the combined effects of acrylic curing, reduction in acrylic thickness, and existence of pores caused by the evolution of gases as the volatiles in the acrylic core are drying.

Introduction

The combination of good vibration damping properties (Refs. 1–3) and high strength-to-weight ratios (Refs. 4–6) make the polymer-cored laminated steels (Fig. 1A) attractive for automotive applications. These materials have been used for the oil-pan, rocker cover, wheelhouse inners and front-dash structures to reduce structure-borne noise and engine noise (Ref. 7). There is some concern, however, that the polymer core may degrade when the laminated steel is exposed to thermal environments. High heat input required from resistance spot welding could also decompose the polymer in the weld nugget. In addition, vehicle structures are often exposed to temperatures ranging from –30°C to 180°C as they encounter paint baking, extreme climatic, and engine/exhaust temperatures. The heat from welding and temperature swings may profoundly affect polymer properties and hence the vibration damping characteristics. Since welded joints are important parts of the body substructure, a fundamental understanding of the damping properties of welded laminated steels is essential.

While there have been a number of studies (Refs. 8–10) conducted to measure the damping behavior of laminated steels, very few data are available on resistance spot welded (RSW) laminated steels. In this study, results from damping property measurements of a RSW acrylic-cored laminated steel, unaged and aged, for varying times at 180°C (Electrophoretic Priming Operation—ELPO temperature) are presented. The role of resistance spot welding in influencing the damping characteristics of a welded acrylic-cored laminated steel at room temperature and at 180°C is also examined. Finally, factors contributing to damping property degradation are identified.

KEY WORDS

Acrylic-Cored Steel
Resistance Spot Weld
Damping Loss Factor
Thermal Aging
Vehicle Noise
Acrylic Adhesive
Weld Schedule
ELPO Treatment
Adhesive Curing

P. C. WANG is with the Manufacturing and Design Systems Dept., General Motors Research and Development Center; and R. J. FRIDRICH is with General Motors Noise and Vibration Center, Warren, Mich.

Experimental Procedure

Material

The laminated steel selected for this study is composed of 0.46 mm (0.018 in.) thick SAE 1006 steel skin and 0.08 mm (0.0032 in.) thick core acrylic adhesive manufactured by Pre Finish Metals, Inc., Elk Grove Village, Ill.

The steel skin contained 0.97 wt-% Mn, 0.48 wt-% C, 0.95 wt-% S, 0.15 wt-% P and 0.10 wt-% Al. The exact formulation of this acrylic adhesive is proprietary to 3M of St. Paul, Minn., but by comparing Fourier Transform Infrared Spectroscopy (FTIR) spectra with reference spectra, the adhesive is believed to be a solvent-based, one-part acrylic consisting of acetate, acrylate, and polystyrene (Ref. 11). Tensile properties of acrylic-cored laminated steel are listed in Table 1.

Since the acrylic core is a good insulator, metallic particles are added to the adhesive for current conduction during resistance spot welding. The nature of these particles is not provided by the manufacturer, so x-ray analyses are performed to obtain the chemical compositions (Ref. 11). Table 2 shows the chemical compositions of the metallic particles.

Specimen Fabrication

The lap-shear specimens, shown in Fig. 1B, were fabricated from 38.1 x 127 mm (1.5 x 5 in.) coupons. Specimens were prepared as follows: 1) bring coupons together; 2) position them with a fixture; and 3) resistance spot weld the specimens. A resistance spot weld with a nugget diameter of 4.8 mm (0.189 in.) was centered on a 38.1 mm (1.5 in.) square overlap region. The weld nugget

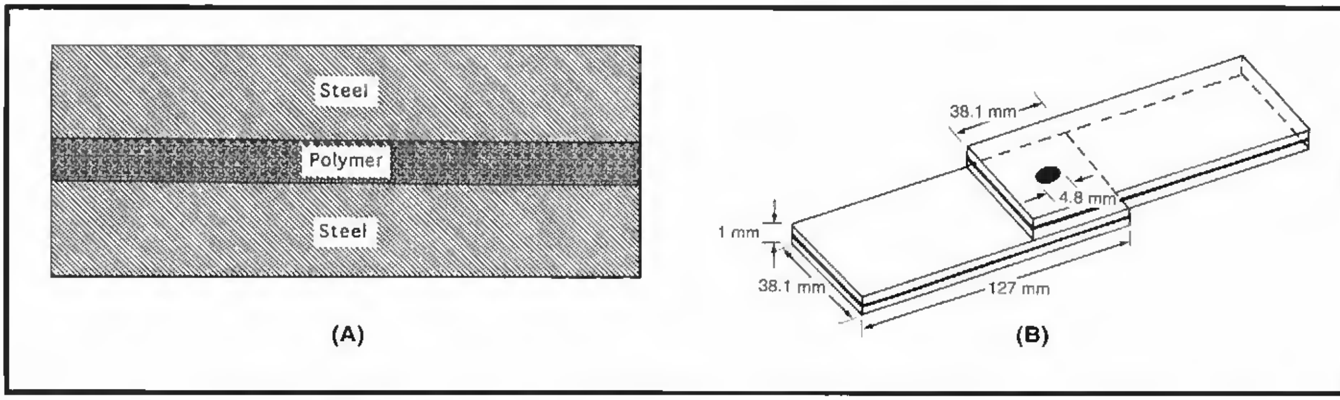

Fig. 1—Schematic of: A—Laminated sheet steel; B—Resistance spot-welded laminated steel.

was prepared using a single-phase, microprocessor-controlled AC 130 KVA (Model Kirkhoff TR49X) press-type spot welding machine, equipped with a Square D 5100 controller. The weld nugget diameter was measured from buttons remaining on specimens that were peel tested in a vise. Minor modifications of the welding current were necessary to maintain the desired weld nugget diameter for all damping samples. The welding schedule employed is given in Table 3.

Thermal Aging

To determine the possible detrimental effect of thermal aging on damping properties, welded laminated steel specimens were exposed in an oven held at 180°C for varying periods of time. Specimens were periodically removed from the oven and cooled to room temperature. The damping properties were measured at room temperature.

Microhardness Measurements

Resistance spot welded specimens were sectioned perpendicular to the sheet thickness and polished so that a hardness traverse could be performed to examine the possible material properties change due to the heat input from welding.

Damping Measurement

The test fixture and instrumentation are shown in Fig. 2. To excite the RSW laminated steel into vibration, a random noise signal from the analyzer's signal generator (power amplifier, Bruel & Kjaer Model 2706) was amplified and sent to the electromagnetic excitation transducer (Electro Model 330HTB) and the first channel of the analyzer (Bruel & Kjaer Model 2032). The response of the RSW laminate to this excitation was measured by a miniature accelerometer (less than 0.5 g, Endevco Model 22), which was mounted to the surface of the specimen using adhesive. The output from the accelerometer was amplified (charge amplifier, Bruel & Kjaer Model 2635) and fed to the second channel of the analyzer. RSW laminated steel has many resonant frequency modes of vibration. To obtain a good measure of damping performance, zoom measurements (In Fast Fourier Transformer (FET) analyzer, the measurement starting with a positive nonzero frequency, *e.g.*, 500–900 Hz, is defined as a zoom measurement.) were made using the analyzer to obtain the detailed frequency response function in a narrow frequency band surrounding each individual resonance. The system loss factor (*i.e.*, the energy dissipation properties of a vibrating system) at a resonant frequency mode is defined in ASTM E756 using the half-power bandwidth method (Ref. 12). By this method, the system loss factor is the ratio of the half-power bandwidth (the width of the response function at a level 3 dB lower than the level at resonance) to the resonant frequency.

Since damping performance varies with temperature and frequency, the fre-

Table 1—Tensile Properties* of Acrylic-Cored Laminated Steel

0.2% Yield strength (MPa)	180
Tensile strength (MPa)	279
% Elongation (in 107 mm)	18.7

*Stroke rate = 0.1 mm/sec.

Table 2—Chemical Composition* of the Particles in Acrylic-Cored Laminated Steel

Fe	Al	Si	Mg	Mn	Cl	Ca	Ti
35	20	30	10	1	2	1	1

*Weight percent.

Table 3—Resistance Spot Welding Parameters

Welding Current (KA)	Welding Time (Cycle)*	Electrode Force (lb)	Electrode Force (N)	Electrode Cap
7.3	8	500	2,224	MWS 6008

*Cycle = 1/60 sec.

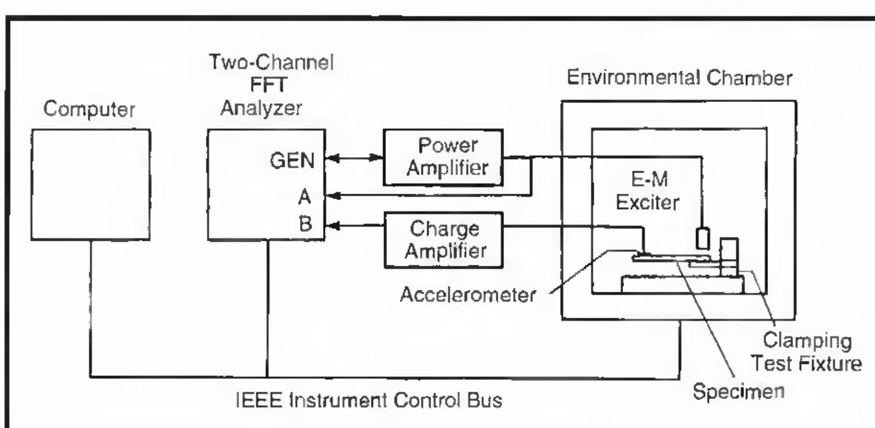

Fig. 2—Damping testing setup.

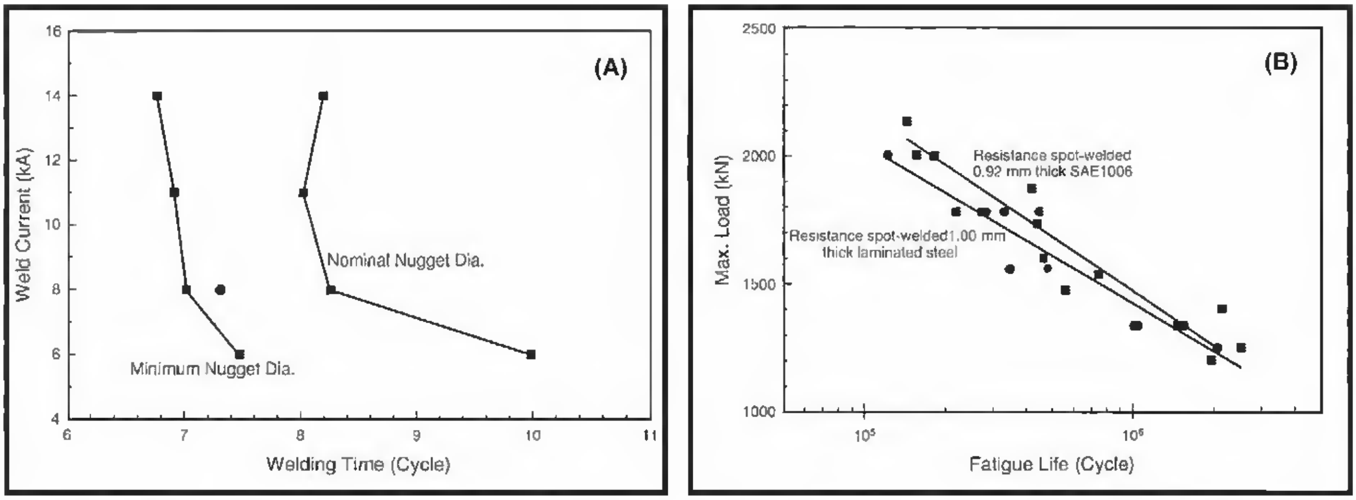

Fig. 3A—Welding lobe diagram for 1-mm-thick acrylic-cored laminated steel; B—Fatigue test results of resistance spot-welded SAE 1006 and acrylic-cored laminated steels.

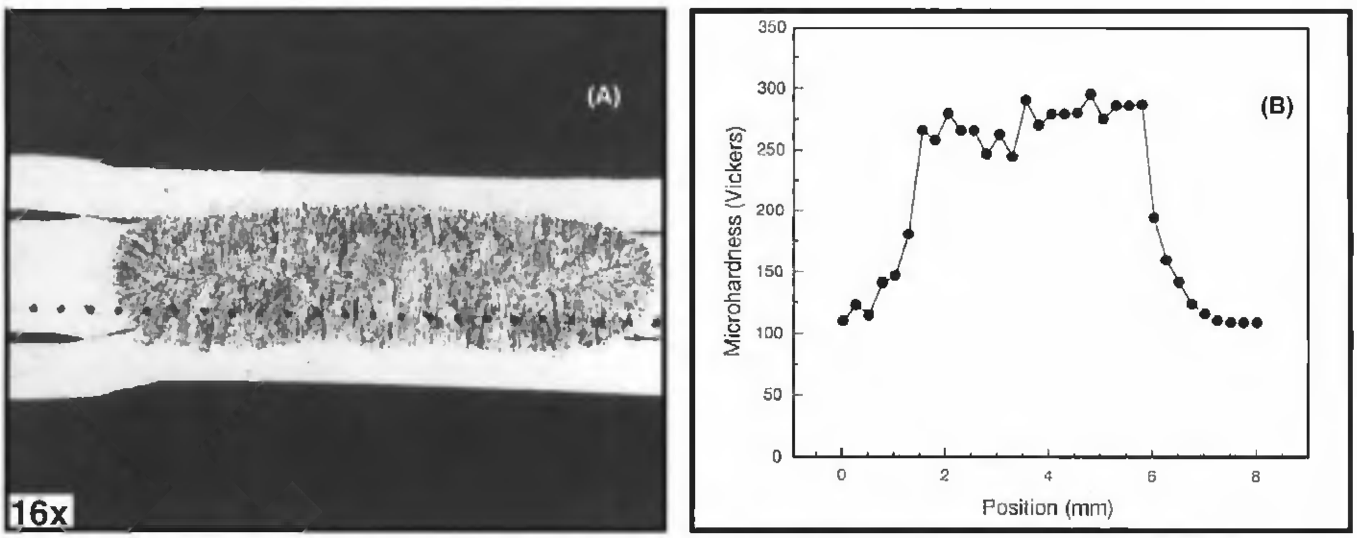

Fig. 4A—A cross section; B—Microhardness of resistance spot-welded acrylic-cored laminated steel.

quency response function measurements of each specimen were repeated over a selected temperature range. Under computer control, measurements were made in the environmental chamber (Cincinnati SubZero Model CT-8-1-H/AC) from –20°C to 80°C in 5°C increments. Before any damping measurements were made at any temperature, the RSW laminate steel was allowed to dwell for no less than 40 minutes once the chamber had reached the desired temperature. This dwell time is required to ensure that the specimens were at thermal equilibrium when the frequency response measurements were made. This dwell time was predetermined by monitoring the temperature of an independent thermocouple attached to a similar RSW specimen during numerous temperature sweeps. Due to the large number of measurements involved (*i.e.*, four aging times and 21 different temperatures), only one specimen was tested in each aging condition.

Thermal Gravimetric Analysis (TGA)

Thermogravimetric analysis on a DuPont 2100 analyzer was used to identify the temperature at which decomposition of the resin takes place. A 40-mg sample of unaged acrylic adhesive was placed in an aluminum pan and the temperature raised to 480°C at a heating rate of 10°C/min.

Differential Scanning Calorimetry (DSC)

Extent of acrylic cure was determined using the 910 DSC unit of a DuPont 2100 Thermal Analyzer under a nitrogen environment. Adhesive specimens were taken from the unaged and aged laminated steels for investigation. Temperature scans were made from –85°C to 250°C at a heating rate of 10°C/min.

Results

Development of Welding Schedule

Although the laminated steels are being mainly used for noise reduction, satisfactory weld strength must be ascertained to meet vehicle structure requirements. Designers can substitute laminated steels for carbon steels in vehicle structural design and achieve equivalent strength performance. Therefore, we used weld strength as the criterion for weld schedule development.

The following procedure was used to determine the welding schedule: 1) resistance spot welding of acrylic-cored laminated steel, 2) conducting the tensile and fatigue tests, 3) comparing the strengths of welded laminated steel and welded SAE 1006, 4) obtaining the desired weld nugget size by adjusting the welding

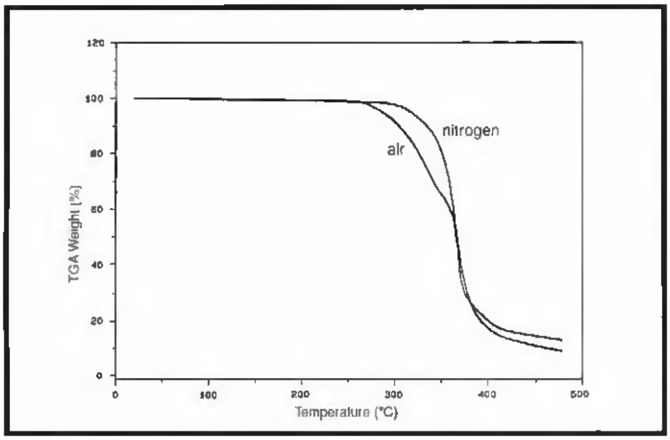

Fig. 5—Thermograms of acrylic adhesive in air and nitrogen.

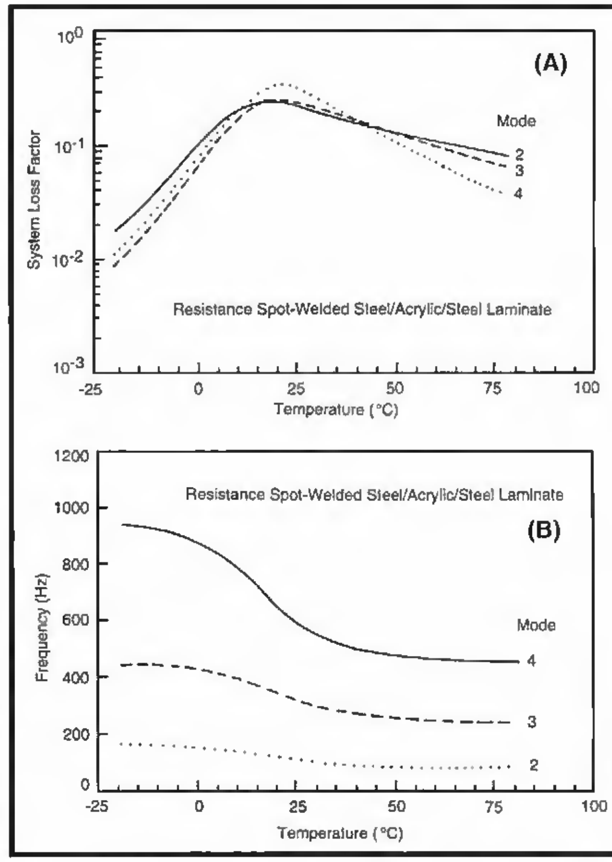

Fig. 6—Variation of: A—System loss factor; B—Resonant frequency with temperature for the resistance spot-welded acrylic-cored laminated steel.

schedule. Extensive welding and testing were performed, and a current range over which spot welds having desirable nugget diameters was obtained for a particular weld time. Figure 3A shows a welding lobe diagram for an acrylic-cored laminated steel. The closed circle in Fig. 3A represents the welding conditions used in specimen fabrication. Figure 3B shows the fatigue strength of RSW laminated steel (filled circle). For comparison purposes, fatigue test results of RSW 0.92 mm (0.036 in.) thick SAE 1006 steel are also included in Fig. 3B. A curve fitting analysis was performed to obtain load vs. life relationship for each specimen type. As shown, no significant difference was found between the fatigue resistance of the RSW laminated steel and SAE 1006 steel. The welding schedule presented here is clearly not a complete representation of various possible welding conditions because it only covers one electrode force, electrode type and electrical current waveform. However, the results of this study showed that welding techniques developed for low-carbon steels can likely be used for the laminated steel without loss in weld quality, provided metallic particles are added to the polymer core to conduct weld current.

Weld Cross Section and Microhardness

A cross-section view of the weld nugget of a resistance spot-welded (RSW) acrylic-cored laminated steel is shown in Fig. 4A. As shown, fusion has progressed to a sufficient distance from the sheet interface to produce a well-defined weld nugget that has penetrated to two-thirds of its final thickness. Results of microhardness traverses along the cross section of a RSW laminate steel are shown in Fig. 4B. Each datum point in Fig. 4B represents an average value from at least two measurements. It can be seen that a high hardness is achieved in the weld nugget, but reduces to lower levels in the heat-affected zone (HAZ). To investigate the effect of joule heat from resistance spot welding on the acrylic adhesive, thermal gravimetric tests were performed. Thermal gravimetric analyses (TGA) of acrylic adhesive in air and nitrogen are shown in Fig. 5. At 180°C, weight losses in air and in nitrogen were identical at about 0.4%, which could be attributed to trapped volatiles and/or residues from incomplete adhesive reaction during fabrication. Rapid decomposition occurs at about 250°C, independent of atmosphere. Above 250°C, the rate of degradation in air was larger than in nitrogen, which is presumably due to oxidation and pyrolysis. Weight losses in air and nitrogen at 480°C were 90.2% and 85%, respectively. Since the melting temperature of SAE 1006 is much higher than 480°C, the joule heat from resistance welding likely causes the acrylic adhesive in the weld nugget region to be completely burned off.

Damping Properties at the Ambient Temperature

Since it is difficult to analyze the first mode (Ref. 12), modes 2 to 4, which are in the frequency range of 50 to 950 Hz, were used for damping measurements. Zoom measurement was performed at each mode. Figure 6A shows the vibra-

Table 4 — Effect of Aging Time on Shear Modulus of the Acrylic-Core Laminated Steel after Aging at 180°C

Aging time (h)	Shear Modulus* (MPa)
0	0.25
0.5	0.36
5.0	3.56
50.0	15.49

*Average of three specimens

Table 5 — Effect of Reduction in Acrylic Thickness on System Loss Factor of the Acrylic-Cored Laminated Steel after Aging at 180°C

Aging time (h)	Acrylic loss factor	Shear modulus (MPa)	Acrylic Thickness (mm)	System Loss factor
0	0.616	0.25	0.025	0.182
0.5	0.616	0.25	0.023	0.176
5.0	0.616	0.25	0.022	0.172
50.0	0.616	0.25	0.020	0.167

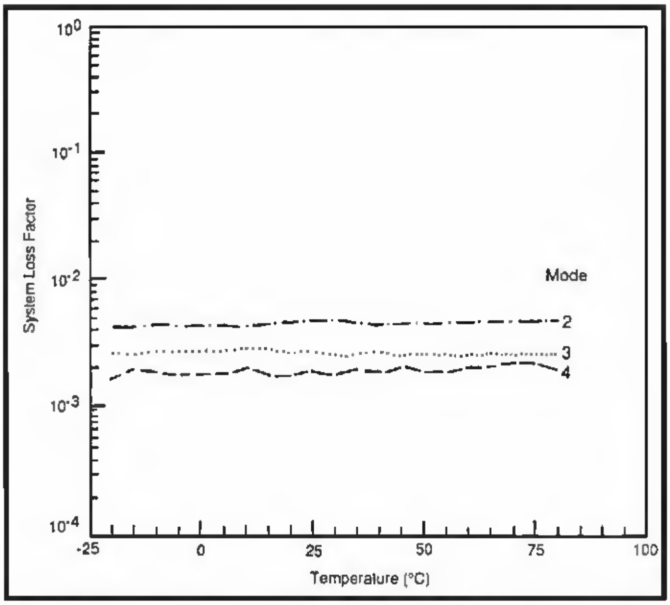

Fig. 7—Damping properties for the resistance spot-welded SAE 1006 steel.

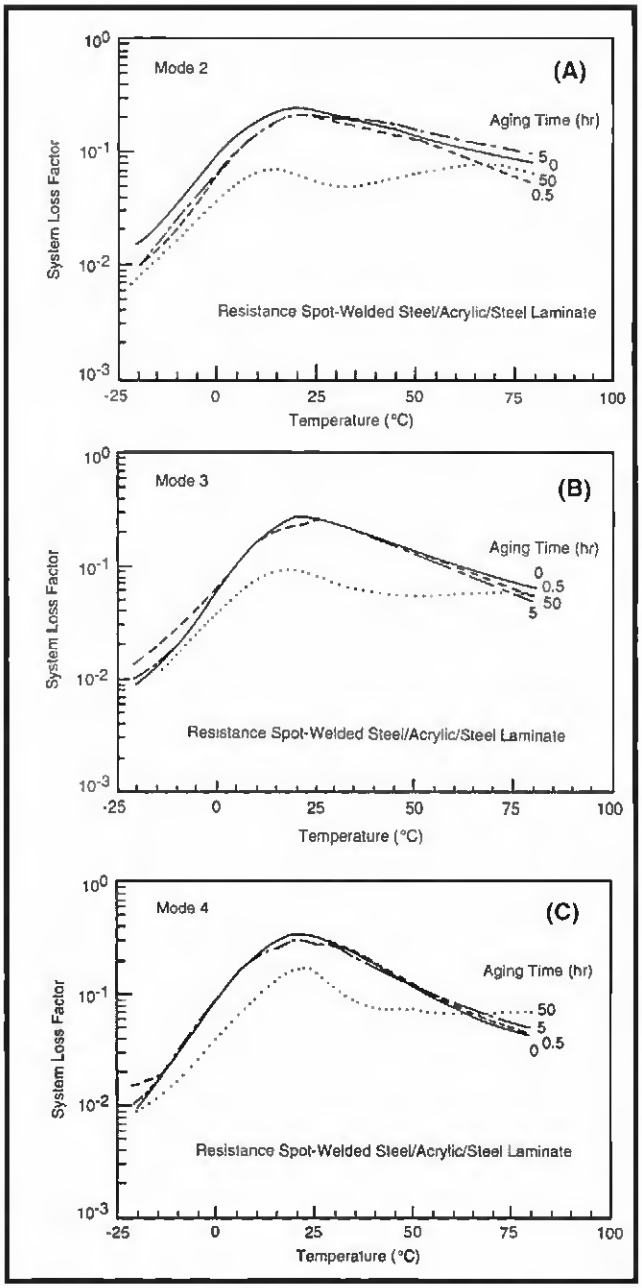

Fig. 8—Effect of thermal aging on the system loss factor of the resistance spot-welded acrylic-cored laminated steel: A—Mode 2; B—Mode 3; and C—Mode 4.

tions of system loss factor (*i.e.*, the energy dissipation properties) vs. temperature for the as-welded laminated steel. As shown, the system loss factor peaks approximately at 20°C, but drops sharply at low and high temperatures. Also, the system loss factor peak height increases with increasing mode number. The value of loss factor peak increases from 0.25 for mode 2 to 0.35 for mode 4. The resonant frequencies vs. temperature for the as-welded laminated steel are shown in Fig. 6B. As the ambient temperature is approached, the RSW laminated steel shows a decreasing frequency as a result of a decrease in stiffness. This is followed by a leveling off or slow decline at higher temperatures.

For comparison purposes, measurements of a resistance spot-welded, bare 1 mm (0.039 in.) gauge low-carbon steel (SAE 1006) are shown in Fig. 7. By comparing Figs. 6 and 7, we see that the system loss factor of RSW SAE 1006 steel was independent of temperature. The system loss factor of the RSW laminated steel was shown to increase one to two orders of magnitude over that of RSW SAE 1006 steel, and the largest gains were made at about 30°C. The improved damping properties of the RSW laminated steel are thought to result from the addition of the adhesive.

Effect of Thermal Aging on Damping Properties

After thermal aging of the RSW laminated steel in an oven held at 180°C and for a predetermined length of time, the system loss factors were measured between –20°C and 80°C, and the results are shown in Figs. 8A–8C. As shown, the positions of system loss factor peak for the unaged, 0.5-, 5- and 50-h exposures at 180°C, and are virtually the same. The peak height did not show any significant reduction after 0.5-h aging; however, the peak height decrease is pronounced in specimens with 50-h aging. The system loss factor reduction is particularly noticeable for mode 2 that has a maximum of about 0.26 for the unaged condition, but drops to about 0.07 after 50 h of aging. The effect of aging on the resonant frequency is shown in

Table 6 — Glass Transition Temperature* and Pore Fraction of Acrylic Adhesive as a Function of Aging Time at 180°C

Aging time (h)	Pore fraction (%)	Glass transition temperature (°C)
0	0	-21.59
0.5	10.0	-21.14
5.0	14.0	-19.14
50.0	11.0	5.67

*Average of two specimens

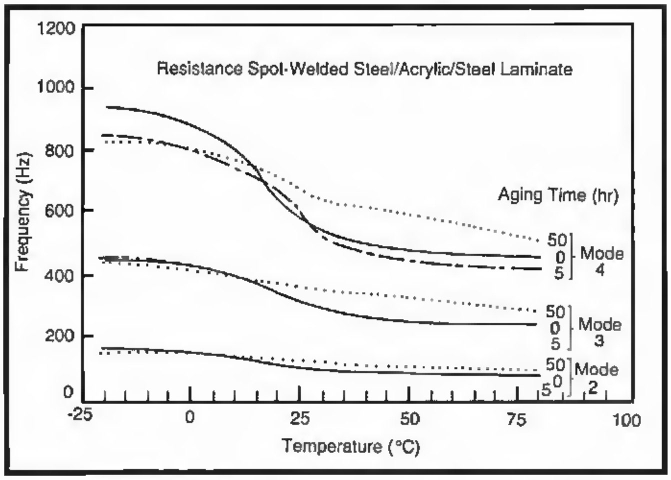

Fig. 9—Effect of thermal aging on the resonant frequency of the resistance spot-welded acrylic-cored laminated steel.

Fig. 9. At low temperature (<15°C), the resonant frequency was essentially unaffected by aging. As the temperature increases, an increase in resonant frequency is observed for modes 2, 3, and 4. By comparing the resonant frequency, it can be seen that the frequency shifts experienced by the modes over the temperature range become less pronounced after 50 h of aging compared to the unaged condition.

Effect of Thermal Aging on Morphology

Since aging at 180°C for 50 h had changed little the microstructures of SAE 1006 steel, we focused on the morphology of the acrylic core. Due to the difficulty in microtomy of acrylic adhesive, scanning electron microscopy (SEM) was used to examine the fracture morphologies of unaged and aged RSW laminated steels. To examine the thermal aging effect on the morphologies of the RSW laminated steel, specimens shown in Fig. 10A were fabricated and exposed in the oven for various aging times and then tested at a strain rate of 0.02 mm/s (0.0008 in./s) at the ambient temperature. Scanning electron micrographs of fractured unaged and aged specimens are shown in Figs. 10B–10E. As shown in Fig. 10B, the unaged adhesive appearance exhibited periodic marking that is preceded and followed by steps, which were relatively flat and almost featureless. However, unlike Fig. 10B, a large number of relatively uniform distributed pores, shown in Figs. 10C–10E, are observed throughout the fracture surfaces for aged specimens.

Measurements of the number and area fraction of pores formed after exposure in air at 180°C for 0.5, 5, and 50 h were made as a function of aging time. A summary of data is shown in Figs. 11A and 11B. As shown in Fig. 11A, within the first 5 h there was an initial increase in average pore size followed by a slight decrease. Similar results were found for the area fraction of pores shown in Fig. 11B. These pores may result from the evolution of gases generated by drying the volatiles. The thicknesses of RSW laminates with various aging times were measured. Figure 12 shows the effect of aging time on the thickness of aged RSW acrylic-cored laminated steel. Each point on the plot represents an average of 15 measurements. Since the steel skin thickness had changed little after aging, the total thickness decrease must be the result of a decrease in acrylic adhesive thickness. Additional experiments were performed to confirm these results. Acylic specimens were placed in an oven held at 180°C for various times and then weighted after removing from the oven. It was found that the mass losses ($(m_o-m_a)/m_o$ where m_o is the original mass and m_a is the mass after aging) were 0.94%, 5.88% and 17.5% for aging times of 0.5, 5 and 50 h, respectively. These results suggest that the thickness change of the acrylic adhesive is likely due to volatile loss.

Table 7 — A Combined Effect of Reduction in Acrylic Thickness and Acrylic Curing on System Loss Factor of the Acrylic-Cored Laminated Steel after Aging at 180°C

Aging time (h)	Acrylic loss factor	Shear modulus (MPa)	Acrylic Thickness (mm)	System loss factor
0	0.616	0.25	0.025	0.182
0.5	0.616	0.36	0.023	0.151
5.0	0.616	3.56	0.022	0.024
50.0	0.616	15.49	0.020	0.006

Discussion

In the previous section, the results of a study of weldability, damping properties, and fracture morphologies of a RSW acrylic-cored laminated steel were presented. In this section, certain aspects of the study are discussed in more detail. These will include the role of resistance spot weld on damping properties, and various factors that degrade the damping properties of RSW laminated steel.

Role of Resistance Spot Weld on the Damping Properties

As shown in Fig. 4, the acrylic adhesive was virtually burned off, and the spot weld nugget was made up of mainly low-carbon steel. The results shown in Fig. 7 indicated that SAE 1006 steel had low damping properties. Thus, one question we must address is whether the resistance spot weld would degrade the damping properties.

The role of spot weld nugget on damping properties can be assessed by comparing the system loss factor of RSW and as-received acrylic-cored laminated steels. Acrylic laminated steel specimens having the same dimensions were fabricated and tested, and results are shown in Fig. 13. For comparison purposes, the results of RSW laminated steel are also included in Fig. 13. As shown, the presence of the weld nugget did not decrease the system loss factor of the RSW joint, indeed the welded joints may have caused a slight increase in the system loss factor of the RSW joint. It was observed that the weld nugget deforms little, and most of the strain energy results from the shearing action within the acrylic core as the laminated steel undergoes bending motion. The damping in RSW laminated steel occurs through a conversion of shear strain energy to heat in the acrylic layer. Energy dissipation arising from relative interfacial slip (Ref. 13) between the upper and lower laminated steel sheets is very small. These results imply that the dominant source of damping is that of the laminated steel, and the weld nugget had little effect on the system loss factor of the RSW laminated steel.

Damping Degradation

The results presented in Fig. 8 demonstrate that RSW acrylic-cored laminated steel degrades when it is exposed at a temperature of 180°C for more than 5 h. Extensive studies indicated that, aside from the composition of the polymer core, three factors ap-

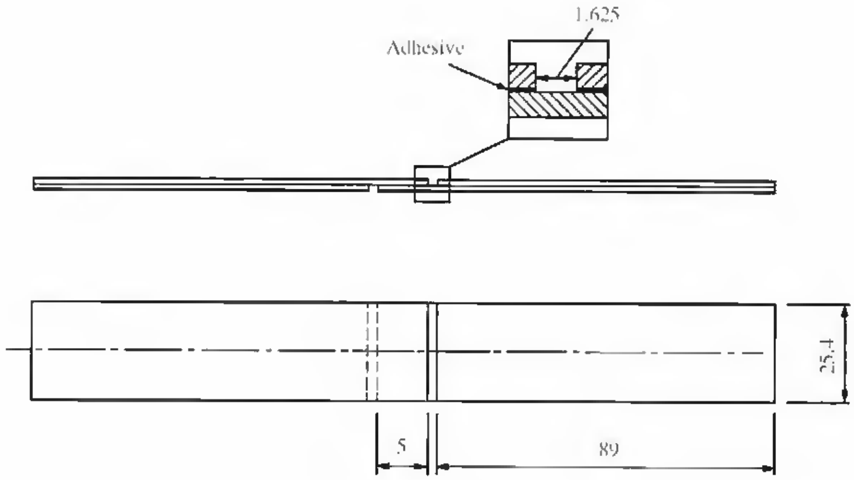

(A)

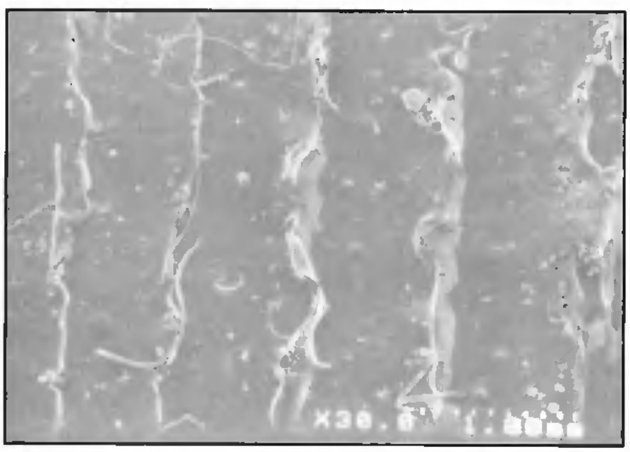

(B)

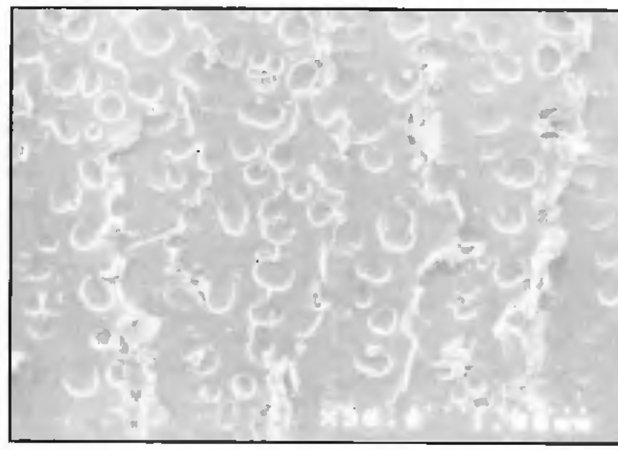

(C)

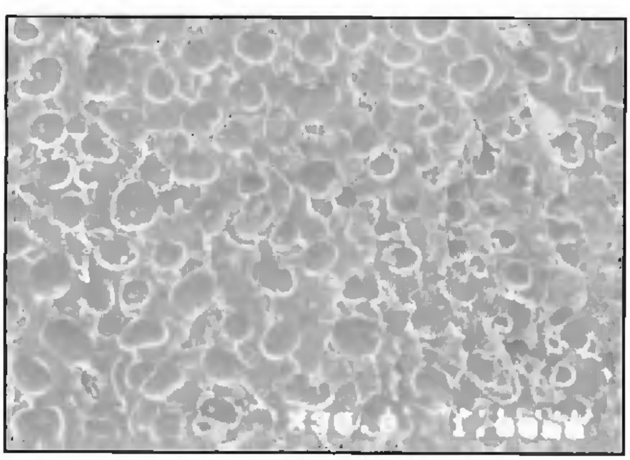

(D)

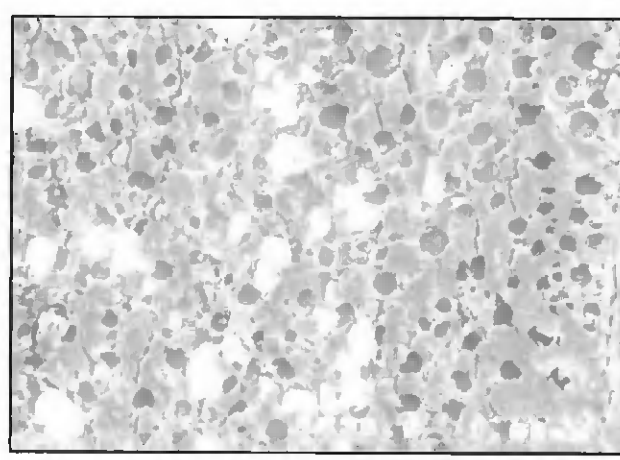

(E)

Fig. 10—A—Shear test specimen (dimensions in millimeters), and scanning electron micrographs of the acrylic adhesive; B—Unaged; C—After 0.5 h; D—5 h; and E—50 h exposure at 180°C.

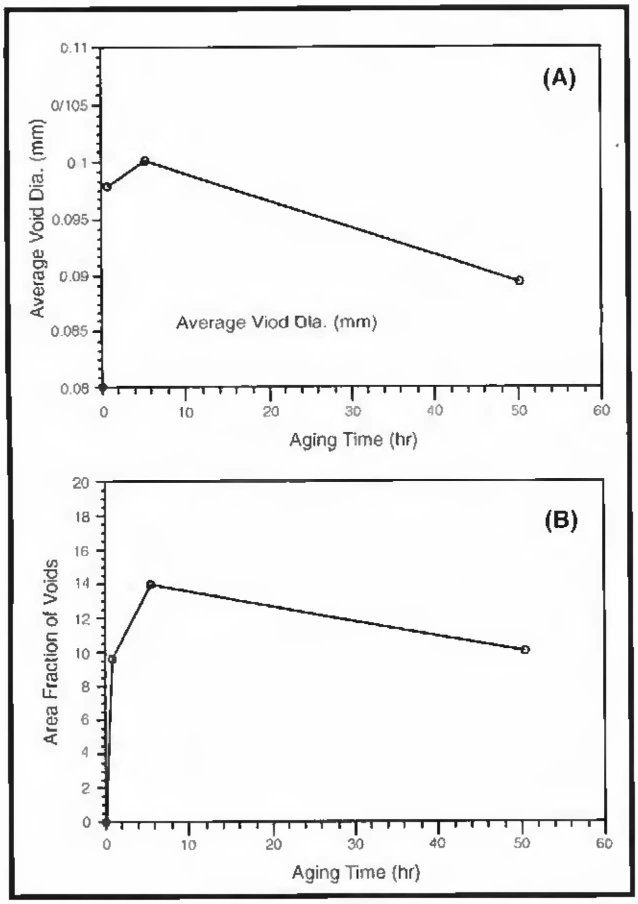

Fig. 11—Pore formation in acrylic adhesive; A—Average pore size, and B—Area fraction of pores as a function of aging time.

the aged RSW acrylic-cored laminated steel: 1) reduction in acrylic thickness, 2) acrylic curing, and 3) evaporation of volatiles. In order to sort out the individual effects of these three contributions to the damping system loss factor, the model developed by Kerwin (Ref. 14) was applied. Kerwin (Ref. 14) has demonstrated that the system loss factor η of a constrained sandwich beam, shown in Fig. 14, is given by the following expressions:

$$h = \frac{(\tan\delta)gY}{1+(2+Y)g+(1+Y)\left[1+(\tan\delta)\right]^2}$$

$$g = \frac{G}{\rho^2 h_2}\left(\frac{1}{E_1h_1}+\frac{1}{E_3h_3}\right)$$

$$\frac{1}{Y} = \left(\frac{E_1h+E_3h_3}{12d^2}\right)\left(\frac{1}{E_1h_1}+\frac{1}{E_3h_3}\right) \qquad (1)$$

where E_1, E_2, and E_3 are the elastic moduli of each layer, G is the real part of the shear modulus of the viscoelastic layer, h_1, h_2, and h_3 are the thicknesses for each layer, d is defined by $d = h_2 + h_1/2 + h_3/2$, ρ is the wave number of vibration ($\rho = 2\pi/\lambda$, where λ is the wavelength), and tan δ is the loss factor of the viscoelastic layer.

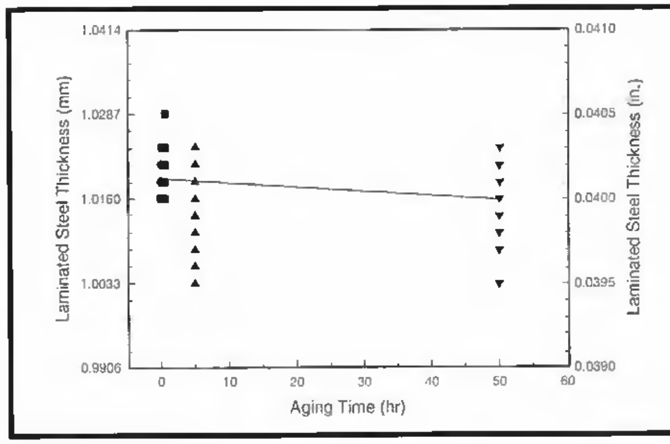

Fig. 12—Effect of thermal aging on the thickness of resistance spot-welded acrylic-cored laminated steel.

The system loss factor of constrained sandwich laminates is governed by the shear energy dissipation of polymer core. It has been suggested that the shear deformation of viscoelastic layer decreases as the core thickness decreases (Refs. 15, 16). Therefore, the observed decrease in system loss factor can be at least partially attributed to changes in acrylic core thickness (Fig. 12) that occurred in thermal aging. To apply Equation 1 necessitates determination of the shear modulus and loss factor of the acrylic adhesive. The shear modulus of acrylic can be determined from the shear stress-strain relationship of acrylic-cored laminated steel specimens (Fig. 10A) and the result is shown in Table 4. The loss factor of the acrylic adhesive can be obtained from the dynamic mechanical analysis (DMA), and the value of loss factor of acrylic adhesive is found to be 0.616 (Ref. 17). The calculated effect of the reduction in acrylic thickness on the system loss factor is shown in Table 5. As shown, a decrease in acrylic core thickness would result in a decrease in system loss factor.

Another contribution to the decrease in system loss factor in RSW-laminated steel is the acrylic cross-linking. It has been shown that acrylic adhesives can cross-link at 100°C (Ref. 18), and the cross-linking increases the storage shear and tensile moduli at the expense of the loss moduli. Differential scanning calorimetry (DSC) measurements of unaged and aged acrylics are shown in Table 6. As shown, aging increased the glass transition temperature (Tg), suggesting that cross-linking developed. The use of Equation 1 for assessing the effect of acrylic cross-linking requires the values of loss factor and shear modulus of the aged acrylic adhesive. To determine the loss factor of the aged acrylic adhesive, aged adhesive needs to be bonded to the aluminum beams by means of an epoxy adhesive (Ref. 19). Since the aged acrylic adhesive was too brittle to press, we were unable to have the undamaged specimens fabricated. Thus, no attempt has been made to determine in this study the loss factor of the aged acrylic adhesive. Instead, the loss factors of the aged acrylic are assumed to be 0.616. Table 7 shows the combined effects of the reduction in acrylic thickness and cross-linking on the system loss factor. As shown, acrylic curing has a strong influence on the damping properties of the laminated steel, with system loss factor decreasing as the aging time increases. It should be noted that the values in Table 7 represent the conservative estimate since the loss factor of the aged acrylic is usually less than that of the unaged acrylic. Comparison of Tables 5 and 7 shows that the degree of system loss factor change by the cross-linking is greater than the reduction in acrylic thickness.

The presence of pores in the acrylic adhesives, shown in Fig. 11, was considered improving the damping properties (Refs. 20–22). Pores in the viscoelastic material convert the longitudinal wave to shear waves. The shear deformation energy is converted to heat by molecular relaxation, and the sound wave is attenuated. As shown in Figs. 11 and 12, and in Table 6, during the first half hour exposure at 180°C, the pore size and fraction grow considerably, while the glass transition temperature increases and acrylic thickness decreases slightly. Therefore, there is a competition among the effects of adhesive curing, reduction in acrylic thickness, and pores. The adverse effects of adhesive curing and core thickness decrease can be reduced in the presence of pores that help in improving the system loss factor. It ends up with little reduction in system loss factor after 0.5-h exposure at 180°C. As the exposure is prolonged, the pore size and fraction decrease. Since the net effect of aging is to decrease the system loss factor, the adhesive curing and reduction in acrylic thickness seem to be the overriding factors. Thus, it is probable that further decrease in system loss factor is considered to be the result of adhesive curing and core thickness reduction during aging.

The results are significant, as they indicate that there is a considerable effect of thermal aging on the acrylic laminated steel. If the temperature-time effect on the material modulus can be expressed by the Arrhenius relationship (*i.e.*, under the assumption that the aging mechanisms, which occur at 180°C, are the same at the lower temperature) (Ref. 23), the effect of a short aging at high temperature on the damping properties may be indistinguishable from that of a long aging at the low temperature. This implies that the damping degradation seen in this study can occur to the material exposed to other elevated temperatures. If this is true, it is recommended that the damping properties of resistance spot-welded acrylic-cored laminate steel used in vehicular structural design be adjusted to account for likely thermal effects.

Conclusions

1) Welding techniques developed for low-carbon steels can also be used for the laminated steel.

2) The damping loss factor of the resistance spot-welded acrylic-cored laminated steel is dominated by the shearing action within the acrylic core. The weld nugget had little influence.

3) Aging resistance spot-welded acrylic-cored laminated steel at 180°C had little effect on the system loss factor for times up to 0.5 h; however, after exposure above 5 h the system loss factor decreased. This decrease in system loss factor is attributed mainly to a combined effect of the acrylic curing, reduction in acrylic thickness, and pores resulting from the evolution of gases generated by drying the volatiles in the acrylic adhesive.

Acknowledgment

The authors wish to acknowledge D. Hayden for microhardness measurements.

References

1. Terashi, S., Asai, M., and Naito, J. 1989. Damping analysis of body panels for vehicle

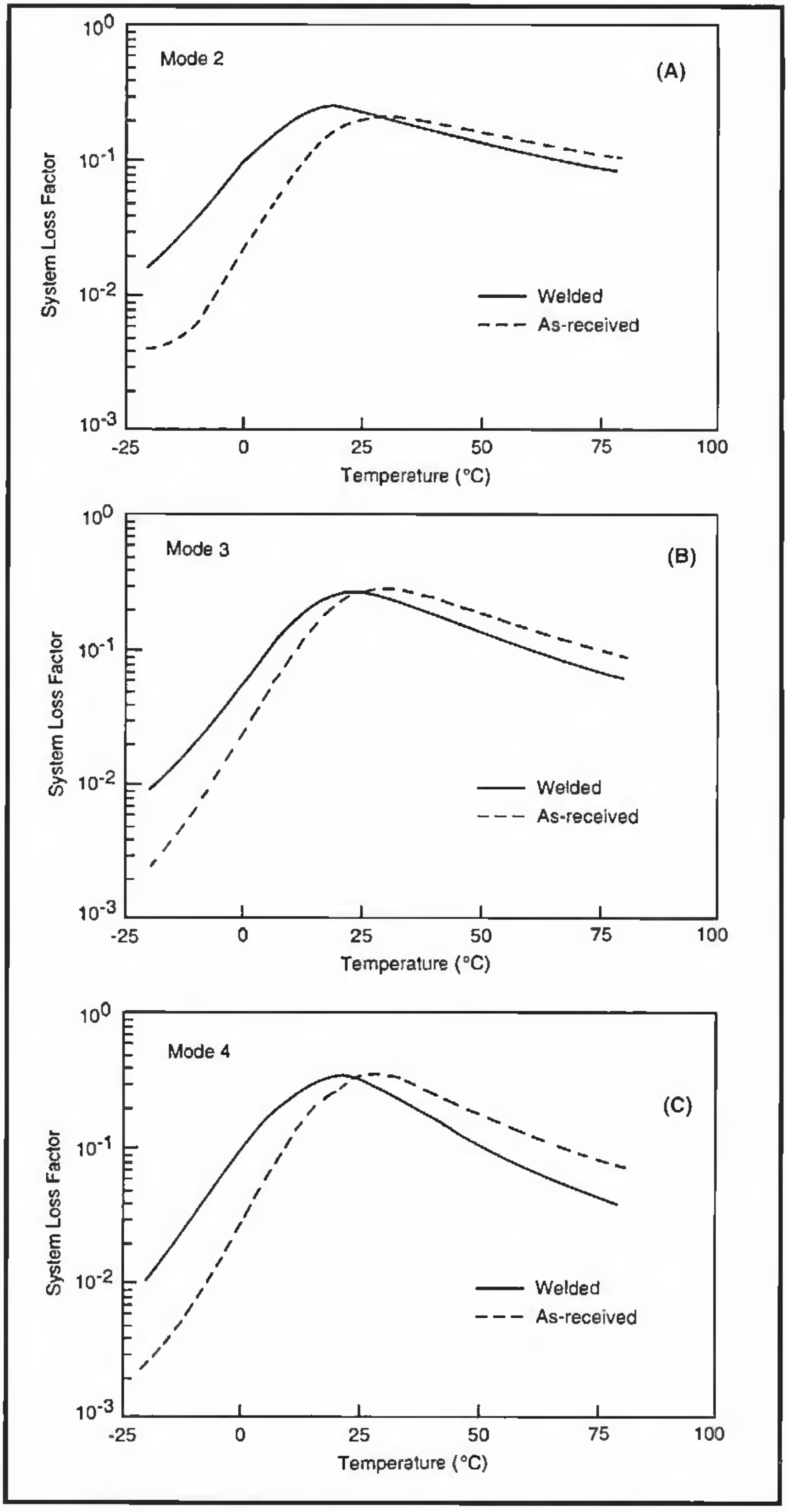

Fig. 13—Variation of system loss factor with temperature for acrylic-cored laminated steel.

RESEARCH/DEVELOPMENT/RESEARCH/DEVELOPMENT/RESEARCH/DEVELOPMENT/RESEARCH/DEVELOPMENT

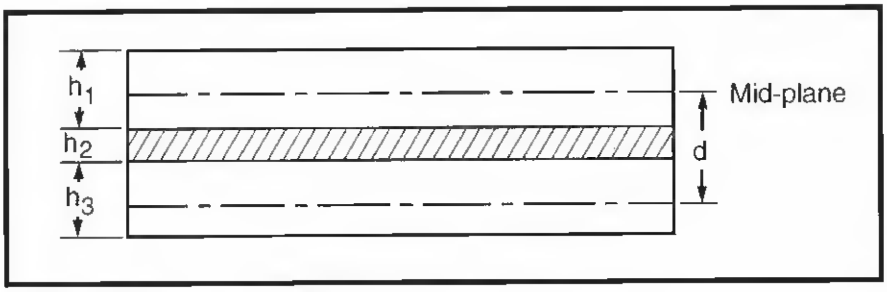

Fig. 14—Nomenclature for the dimensions of a constrained sandwich beam.

interior noise reduction. *Society of Automotive Engineers, Paper 891135,* International Congress and Exposition, Detroit, Mich.

2. Shiroi, Y., Niwa, S., and Iwata, T. 1989. Application study of vibration damping composite steel sheet to the car body. *Society of Automotive Engineers, Paper 890613,* International Congress and Exposition, Detroit, Mich.

3. Suzukawa, Y., Ikeda, K., Morita, J., and Katoh, A. 1992. Application of vibration damping steel sheet for automotive structural parts. *Society of Automotive Engineers, Paper 920249,* presented at the International Congress and Exposition, Detroit, Mich.

4. DiCello, J. A. 1980. Steel-polypropylene-steel laminate—a new weight reduction material. *Society of Automotive Engineers, Paper 800078,* International Congress and Exposition, Detroit, Mich.

5. Miller, W. K. 1980. Metal-plastic laminates for vehicle reduction. *Society of Automotive Engineers, Paper 800077,* International Congress and Exposition, Detroit, Mich.

6. McKenna, L. W., Wohl, M. H., and Woodbery, J. C. 1980. New light weight material for vehicle body panels aluminum/nylon laminates. *Society of Automotive Engineers, Paper 800079,* International Congress and Exposition, Detroit, Mich.

7. Vydra, E. J. 1993. Composite for noise reduction. *Automotive Body Materials,* Proceedings of the 1st International Body Engineering Conference, 79–80, Detroit, Mich.

8. Watanabe, Y., Takeda, T., Kabasawa, M., Tanabe, S., and Yoshida, M. 1985. Development of vibration-damping sheets. *Society of Automotive Engineers, Paper 850325,* International Congress and Exposition, Detroit, Mich.

9. Sakai, K., Fujiwara, H., and Sato, M. 1982. Damping composite sheet for noise control. *Society of Automotive Engineers, Paper 820752,* International Congress and Exposition, Detroit, Mich.

10. Murase, M., Mukaihara, F., Izawa, M. Natures, Y., and Ichida, T. 1993. Development of vibration damping steel sheets for automotive oil pans. *Society of Automotive Engineers, Paper 930023,* International Congress and Exposition, Detroit, Mich.

11. Wang, P. C. 1994. Identification and analysis of acrylic-cored laminated steel. Unpublished work, General Motors Corporation.

12. ASTM Standard E756-93. 1993. Standard method for measuring vibration-damping properties of materials.

13. Beards, C. F. 1983. The damping of structural vibration by controlled interfacial lip in joints. *Journal of Vibration, Acoustics, Stress, and Reliability in Design,* ASME, 105: 369–373.

14. Kerwin, E. M. 1959. *Journal of Acoustical Society of America,* 31: 952.

15. Ungar, E. E., and Kerwin, E. M., 1962. Loss factor of viscoelastic systems in terms of energy concepts. Journal of Acoustical Society of America, 34: 954–957.

16. Grootenhuis, P. 1970. The control of vibrations with viscoelastic materials. *Journal of Sound Vibration,* 11(4): 421–433.

17. Schwaeger, J. 1994. Pre Finish Metals, Inc., Elk Grove Village, Ill., private communication.

18. Kordzinski, S., and Horn, M. B. 1971. U. S. patent 3,579,490.

19. Lewis, T. M., and Branch, R. D. 1987. Routine damping material and design of surface damping treatments. Society of Automotive Engineers, Paper 870986, Presented at the International Congress and Exposition. Detroit, Mich.

20. Meyer, E., Brendel, K., and Tamm, K. 1958. *Journal of Acoustical Society of America,* 30: 1116.

21. Meyer, E. 1970. *Applied Acoustics,* 3: 169.

22. Oberst, H. 1957. Resonant sound-absorbers. *Technical Aspects of Sound,* Richardson, E. G., (ed.), Elsevier Publishing Co., New York.

23. Maron, S. H., and Prutton, C. F. 1965. *Principles of Physical Chemistry,* Macmillan & Co., New York, N.Y.